

Diffusion mechanisms of Mo contamination in Si

D. S. Lambert¹, A. Lennon¹, and P. A. Burr²

¹*School of Photovoltaics and Renewable Energy Engineering, UNSW Sydney, Kensington, NSW 2052, Australia*

²*School of Mechanical and Manufacturing Engineering, UNSW Sydney, Kensington, NSW 2052, Australia*



(Received 25 September 2019; accepted 14 January 2020; published 10 February 2020)

Molybdenum contamination of silicon can have serious detrimental consequences for the efficiency of solar cells, raising durability concerns for novel solar cell designs that utilize MoO₃ in contact with Si. Density functional theory simulations of Mo defects in Si revealed that Mo is preferentially accommodated in tetrahedrally coordinated interstitial sites and that the contamination may reach a sufficiently high concentration to cause a 20% relative solar cell efficiency degradation if processing steps are performed between 950 and 1300 K. The formation energy of the most energetically favored Mo defect in Si has a minimum value of 1.58 eV at the valence band maximum and a maximum of 2.10 eV at higher Fermi levels, indicating that higher Mo defect concentrations may occur in *p*-type Si than intrinsic or *n*-type Si. The diffusion processes for Mo in Si were investigated, and it was identified that interstitial diffusion dominates over a vacancy-mediated mechanism under all equilibrium conditions. Migration barriers were calculated to be 2.29 eV for charge neutral and 2.03 eV for charge +1 defects, occurring under *n*-type and *p*-type doping, respectively, indicating that Mo diffusion is faster in *p*-type Si, and hence potentially more effectively gettered than it would be in *n*-type Si.

DOI: [10.1103/PhysRevMaterials.4.025403](https://doi.org/10.1103/PhysRevMaterials.4.025403)

I. INTRODUCTION

Molybdenum contamination of Si is a matter of great concern for a number of device applications, with particularly severe consequences for solar cell applications. Davis *et al.* [1] identified that out of 14 different impurities in Si, Mo was the second most deleterious impurity species for a given concentration, with a concentration of 10¹² atoms/cm³ (20 ppt) causing ~20% reduction in relative efficiency. This was also confirmed by Rohatgi *et al.* [2], who reported that relative cell efficiency reductions between 18 and 28% occurred due to Mo defect concentrations greater than 10¹² atoms/cm³. However, Coletti *et al.* [3] subsequently reported that the negative impact of Mo on more recent cell designs, which depend on higher minority carrier lifetimes for high voltages, starts at concentrations above 10¹¹ atoms/cm³. This Mo-induced degradation is due to the formation of deep level states, approximately 0.3 eV above the valence band maximum (VBM) [2,4–6], with a high electron capture cross section [2] resulting in high levels of carrier recombination [7].

Molybdenum contamination, with concentrations above this harmful threshold, have been reported in multicrystalline Si used for industrial solar cells, the Mo not being completely removed during the initial metallurgical purification of Si [8]. There has also been increasing interest in recent years in using MoO₃ layers in contact with Si as carrier-selective contacts for hole extraction [9,10]. This hole collection method can reduce parasitic absorption compared to equivalent doped a-Si heterojunction cells and has resulted in reported cell efficiencies of up to 22.5% [10]. The use of Mo-containing thin films in such close contact with the Si absorber raises further concern about the potential contamination of the substrate Si from interdiffusion of Mo from the MoO₃ carrier-selective contact layer. Furthermore, unlike other common Si contaminants like

Fe, Mo is difficult to getter in solar cells because of its low diffusivity in Si [11].

While other transition metal impurities in Si have been investigated with first principles methods [12,13], almost no density functional theory (DFT) reports of Mo defects in Si have been published, with the only exception appearing to be a single study by Marinopoulos *et al.* [14], which calculated electrical transition states and interstitial migration energies of Mo and five other transition metal impurities in Si. Marinopoulos *et al.* made the assumption that the stable hexagonal defect is a reasonable approximation for the transition state of a jump between two adjacent tetrahedral sites. Our study first validates the chosen computational parameters against previous results, then expands the current understanding of Mo impurities in monocrystalline Si by determining the probability of substitutional and interstitial Mo defects in Si, under all relevant oxidation levels and their predicted concentrations, and by providing a detailed understanding of their mechanisms of diffusion.

II. METHODOLOGY

A. Defect formation energy and concentration predictions

Formation energies are calculated with the following equation:

$$E_f = E_{\text{defect}} - E_{\text{host}} + \sum_j \Delta n_j \mu_j + q(E_{\text{VBM}} + \mu_e) + E_{\text{chgor}}, \quad (1)$$

where E_{defect} and E_{host} are the DFT energies of the defective and perfect supercells, the summation term refers to the chemical potential μ of removed (Δn positive) or added (Δn negative) atoms, and the fourth term accounts for the chemical potentials of added/removed electrons, being the sum of the

Fermi energy μ_e (relative to the VBM) and E_{VBM} , the energy of electrons at the VBM. The chemical potentials μ_{Si} and μ_{Mo} were taken from the DFT energy per atom of crystalline Si and metallic (bcc) Mo, consistent with the method of previous studies on other transition metals in Si [15,16]. E_{chgor} refers to the charge correction required to counter the electrostatic defect-defect self-interaction in finite systems with periodic boundary conditions. A first order charge correction was applied, given by [17]

$$E_{\text{chgor}} = \frac{q^2\alpha}{2\epsilon L}, \quad (2)$$

using a DFT calculated dielectric constant of Si of $\epsilon = 12.9$, close to the experimental value of 11.7 [18]. Due to the large supercell used and the high dielectric constant, the required charge correction was not large, with corrections of less than 0.14 eV for +4 charge defects being the highest charge considered in the current study.

The defect formation energy is related to the equilibrium concentration of the defect through an Arrhenius relationship [19]:

$$c_i = m_i \exp\left(\frac{-\Delta E_f^i}{kT}\right), \quad (3)$$

where m_i is the multiplicity of the defect with respect to that of Si sites in the crystal lattice, and ΔE_f^i is the defect formation energy as calculated with Eq. (1). This relation was used to predict defect concentrations under different temperature conditions.

B. Single-jump diffusion calculations

Diffusion of chemical species in a crystal can be described as a Markov chain of jumps (stochastic, memoryless) from one lattice site to the others. In some cases, the jumps involved in the migration process are all symmetrically equivalent, and diffusion occurs through a repetition of the same jump type. An example of such diffusion process is that of a vacancy in a cubic crystal, such as Si, in the absence of any other defects. In some cases, interstitial species may also diffuse through a single-jump mechanism, as is the case for Mo in Si.

For species that can diffuse in a crystal through the repetition of a single (isotropic) jump, the diffusivity is given by [20]

$$D_{\text{inter}} = (1/6)f_0gl^2\omega_i, \quad (4)$$

where g is the number of equivalent diffusion jumps, f_0 is the geometric correlation factor, l is the jump length, and ω_i is the successful jump frequency, formulated in terms of the jump barrier height according to [21]

$$\omega_i = v^* \exp\left(\frac{-\Delta H_m}{k_B T}\right), \quad (5)$$

where ΔH_m is the barrier height of the jump, calculated with the nudged elastic band (NEB) technique [22], and v^* is the attempt frequency, which can be calculated using the

(harmonic) Vineyard approximation [23] as

$$v^* = \prod_{i=1}^{3N-3} v_i \bigg/ \prod_{j=1}^{3N-4} v'_j, \quad (6)$$

where v_i and v'_j are the vibrational frequencies of every atom at the initial jump site and at the transition site of the jump, respectively, which can be calculated in DFT [24]. To simplify the calculation, a number of studies [25–28] have used the hopping atom approximation where only the vibrational frequencies of the hopping atom are calculated. This is a reasonable approximation as the other atom frequencies tend to cancel out and reduce the numerical error arising from dividing large numbers by similarly large numbers [26]. Note that in the transition state, which is by definition on a saddle point in the energy surface, one vibrational frequency must be imaginary, thus the denominator of Eq. (6) is summed over all real frequencies only.

C. Vacancy-mediated diffusion

The calculation of substitutional solute diffusion is more complicated than the case of single-jump diffusion. Most commonly, substitutional atoms diffuse through a vacancy-mediated process [29], requiring the presence of another vacancy in the host material to give the defect space to move. For an individual solute hop, the vacancy must make several jumps to approach the solute atom and then a further jump to exchange position. Structural and electronic distortions caused by the solute means that, in the vicinity of the solute, symmetry is broken and each of these jumps will have different characteristics.

The jump network for a solute vacancy interaction for the diamond structure is shown in Fig. 1. For the calculation of diffusivity, the four-frequency model is used [30,31] with the assumption that solute-vacancy interaction become negligible beyond the 2 nn configuration. The ω_0 frequency is that of a dilute vacancy jump in the absence of, or far away from, any defects. The ω_2 frequency is that of the exchange jump where the solute atom (in position S) exchanges places with a neighboring vacancy (in position 1 nn). The jump away from the first nearest neighbor interaction has frequency ω_3 ; and the reverse jump of ω_3 is referred to as ω_4 . Further jumps out to the 3 nn and 5 nn site and beyond are assumed to be equal to ω_0 . Note that unlike the five frequency formulation [21] commonly used for FCC lattices, in the diamond structure there is no reconfiguration jump (called ω_1 in the five-frequency model), where the vacancy migrates from a 1 nn site to a different 1 nn site.

The tracer self-diffusion coefficient for a crystal is given by [32]

$$D_{\text{self}} = f_0 C_v l^2 \omega_0, \quad (7)$$

where f_0 is the geometric correlation factor, C_v is the concentration of vacancies, l is the jump length, and ω_0 is the successful jump frequency.

The diffusivity for a vacancy-mediated solute, $D_{\text{vacmediated}}$, is closely related to the vacancy self-diffusivity of a tracer

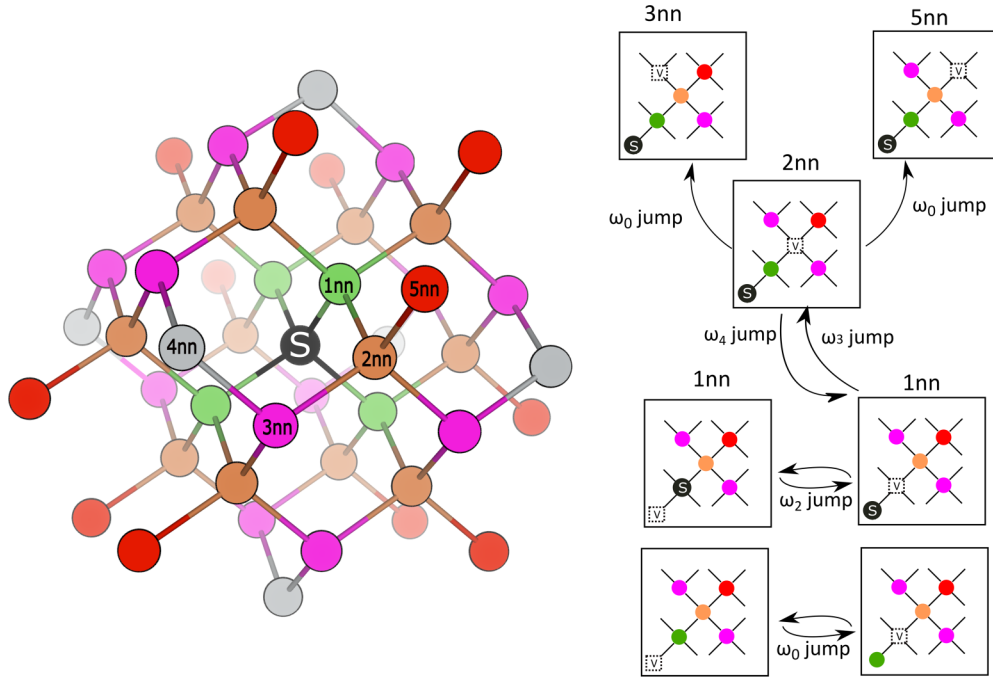


FIG. 1. Illustration of the jump network for vacancy-mediated diffusion in diamond. (left) Color coding represents equivalent sites relative to a central solute S (in grey), sites labeled in order of increasing distance away from the solute. (right) Labeling of the jumps used in the four-frequency model.

atom, D_{self} , and can be calculated as [21,33]

$$\frac{D_{\text{vacmediated}}}{D_{\text{self}}} = \frac{f_2 \omega_4 \omega_2}{f_0 \omega_0 \omega_3}, \quad (8)$$

where the geometric factor f_2 depends on the individual jump frequencies, as well as the geometry of the specific crystal, f_0 is the correlation factor of tracer self-diffusion and each ω frequency is calculated from its corresponding migration barrier and preexponential factors using Eq. (5). When combined with Eq. (7) the solute diffusivity becomes [34]

$$D_{\text{vacmediated}} = f_2 \omega_2 l^2 C_v \frac{\omega_4}{\omega_3}. \quad (9)$$

One reasonable assumption to make for these calculations is that the attempt frequency of all the vacancy jumps except ω_2 (solute exchange) are equal to that of the vacancy self-diffusion jump [35]. In the diamond lattice, the correlation factor f_2 can be calculated with [31]

$$f_2 = \frac{3F \omega_3}{3F \omega_3 + 2\omega_2}, \quad (10)$$

where F is a weighting term that depends on the individual jump frequencies, analytically approximated to be [30]

$$F = \frac{8.71 + 15.36\alpha + 6.29\alpha^2}{8.71 + 19.7\alpha + 13.83\alpha^2 + 3\alpha^3}, \quad (11)$$

where α is $\alpha = \omega_4/\omega_0$.

D. Computational details

All DFT calculations were performed using the VASP software package. PAW pseudopotentials were used with a cutoff energy of 350 eV, using 4 and 14 valence electrons for Si and Mo, respectively, in conjunction with the PBE

exchange-correlation functional. All defects were calculated in 216-atom supercells, and the Brillouin zone sampling was performed with a k -point grid of $3 \times 3 \times 3$. Defects were relaxed at constant volume. These parameters are in line with the state-of-the-art of DFT simulations in Si; see Table I [14–16,36–48]. The electronic energy convergence criteria was 2×10^{-7} eV, and for ionic steps the convergence criterion was a change in energy of less than 10^{-5} eV.

Marinopoulos *et al.* [14] found that the application of a self-consistent +U parameter [49] to Mo defects in Si did not lead to any improvement in the accuracy of describing migration barriers or electrical levels properties. For this reason, no +U parameter was used for calculations reported in this study.

Diffusivity jumps were calculated with the NEB method, with a force convergence criteria of less than 10^{-2} eV/Å. Electronic DOS calculations were performed through single point recalculations of relaxed PBE structures using the tetrahedron smearing method with Blöchl corrections [50].

E. Defect formation energies and concentrations

The three stable Si self-interstitial sites are the tetrahedral site, the hexagonal site and the split $\langle 110 \rangle$ site [45], as shown in Fig. 2. The tetrahedral site has four Si neighbors at an equal distance of 2.35 Å. The hexagonal site is halfway between two tetrahedral sites, having six nearby Si atoms on a nearly planar arrangement at a distance of 2.25 Å. Last, there is the split $\langle 110 \rangle$ interstitial, where one single Si atom is replaced by two Si atoms displaced along the $\langle 110 \rangle$ direction.

The formation energies of the self-interstitial defects, as well as Si vacancies are shown in Fig. 3. Note that the Fermi

TABLE I. Comparison of computational parameters for selected DFT studies investigated defects in Si.

Year	Authors	XC function	Number of atoms	k -points	Defect studied
1999	Leung <i>et al.</i> [45]	LDA, PW91	16, 54, 128	N/A	Intrinsic
2003	Probert and Payne [44]	PW91	16	$2 \times 2 \times 2$	Intrinsic
2004	Mo <i>et al.</i> [46]	LDA	216	1	S
2006	Batista <i>et al.</i> [47]	TPSS, HSE, PW91	16	$8 \times 8 \times 8$	Intrinsic
2006	Wright [48]	LDA, PBE	216, 512, 1000	Various	Intrinsic
2008	Zhang <i>et al.</i> [15]	PW91	32, 64	$4 \times 4 \times 4$	V, Cr, Mn, Fe, Co, Ni
2009	Rinke <i>et al.</i> [43]	LDA, LDA+GW	64	$3 \times 3 \times 3$	Intrinsic
2011	Corsetti and Mostofi [42]	LDA	2–256	various	Intrinsic
2011	Estreicher <i>et al.</i> [41]	LDA, PBE, RevPBE	64	$2 \times 2 \times 2$	Intrinsic, H, Fe, Ni, O
2014	Legrain <i>et al.</i> [40]	PBE	64	$3 \times 3 \times 3$	Li Na, Mg
2015	Marinopoulos <i>et al.</i> [14]	PBE+U	512	1	Ti, V, Cr, Zr, Nb, Mo
2015	Dabrowski <i>et al.</i> [39]	PBE	8–1458	Various	Intrinsic
2016	Backlund <i>et al.</i> [38]	RPBE	216, 64	$3 \times 3 \times 3$	Intrinsic, V, H
2016	Du <i>et al.</i> [37]	PBE	64, 96, 216	$4 \times 4 \times 4$	S, Se, Te
2017	Sharan <i>et al.</i> [16]	HSE06	64	$2 \times 2 \times 2$	Cu, Cu+H
2019	Tsuchiya <i>et al.</i> [36]	PBE	64	$2 \times 2 \times 2$	Intrinsic, C, O, P
	Current work	PBE	216	$3 \times 3 \times 3$	Intrinsic, Mo, Mo + (H, P, B, Cu, O)

level range was limited to the DFT band gap value of 0.67 eV (similar to previous research [37,51]) for the sake of internal consistency. At low Fermi levels, the tetrahedral site is the most favored, while at the highest Fermi levels the charge neutral split $\langle 110 \rangle$ interstitial becomes slightly favored, consistent with LDA calculations undertaken by Rinke *et al.* [43] The +1, +2 and +4 charges of the interstitial defect in the hexagonal site were found to not be stable, collapsing onto the tetrahedral site. The magnitudes of the charge neutral interstitial defects are also similar (within 0.4 eV) of previous studies [43,45,52]. The results for the Si vacancy also fall within the range of literature values, and lie within 0.13 eV of those obtained by Wright *et al.* [48] from 1000-atom supercell with fine k -point sampling, providing further confidence in the computational method.

All interstitial sites that were found to be stable for Si self-interstitials were investigated for Mo_i defects. Both the tetrahedral and hexagonal sites were found to be stable, while the split $\langle 110 \rangle$ defect (with one Mo atom and one Si atom) was not stable, collapsing onto the tetrahedral Mo interstitial site. To ensure these were the only stable sites, a number of other sites were tested in a smaller 64 atom Si supercell (with a $2 \times 2 \times 2$ k -point sampling grid). Ten symmetry-unique sites were identified whose equivalent sites tile the whole unit cell along an $8 \times 8 \times 8$ grid. The

mid-bond site between two Si atoms was disregarded as the Mo atoms are too large to fit in this site. Simulations with Mo defects at all other sites were attempted to determine if any of these sites were stable. Of the Mo defects on the nine remaining sites, seven collapsed onto the tetrahedral arrangement, and two collapsed onto the hexagonal arrangement, confirming that these are the only stable sites for Mo interstitials.

The formation energies of Mo interstitial and substitutional defects are shown in Fig. 4. Defects at the two interstitial sites exhibit similar charge behavior, being +3 charged when the Fermi level is at the VBM and then becoming charge neutral at higher Fermi levels. The energy at which Mo interstitials switch from charge neutral to charge +1 states is 0.30 eV, which matches very well with experimental reports of the Mo(0|+) transition energy at 0.3 eV [2,53,54], and with previous DFT value of 0.31 eV reported by Marinopoulos *et al.* [14] There do not appear to be any previous reports of Mo_i becoming +2 or +3 charged, which is predicted to occur here. This implies that these sites have either failed to be captured in the literature, or that they arise from known limitations of the PBE functional (e.g., due to delocalisation). The Mo_{Si} defects, which are consistently less favorable than Mo_{i(tet)}, are charge neutral at low Fermi levels but switch to a -1 charge as the Fermi level increases.

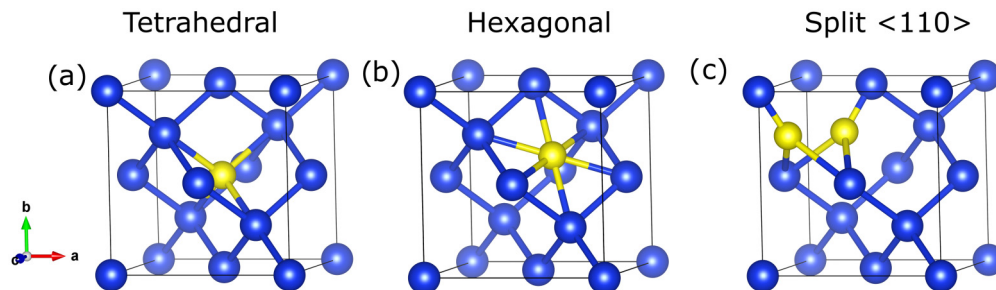


FIG. 2. Illustration of the three stable sites for Si interstitials: (a) interstitial in tetrahedral site, (b) interstitial in hexagonal site, and (c) split $\langle 110 \rangle$ site.

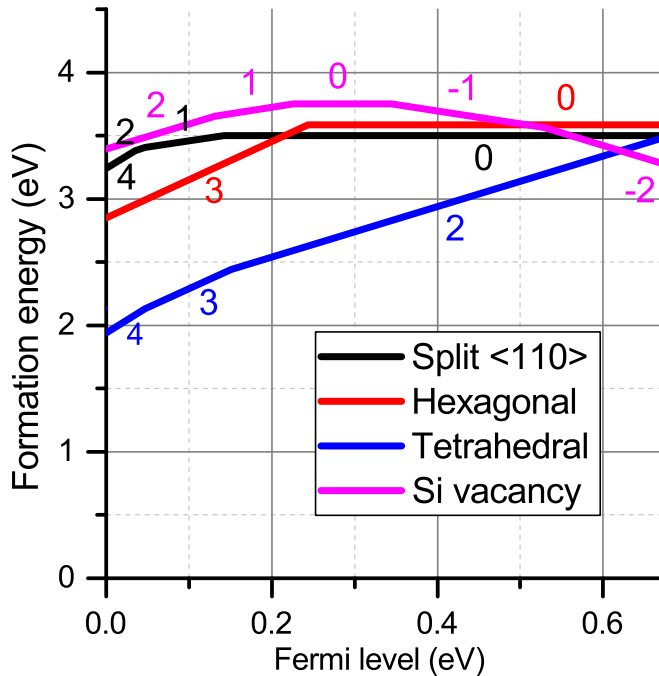


FIG. 3. The formation energy of the dominantly charged intrinsic defects at each Fermi level in Si. The charge state of the most favored charge of each defect is labeled.

These results can be compared to that of other transition metals reported in a PBE DFT study of charge-neutral defects by Zhang *et al.* [15], with the ordering of charge-neutral defects for Mo matching V, Cr, and Fe, with a magnitude most

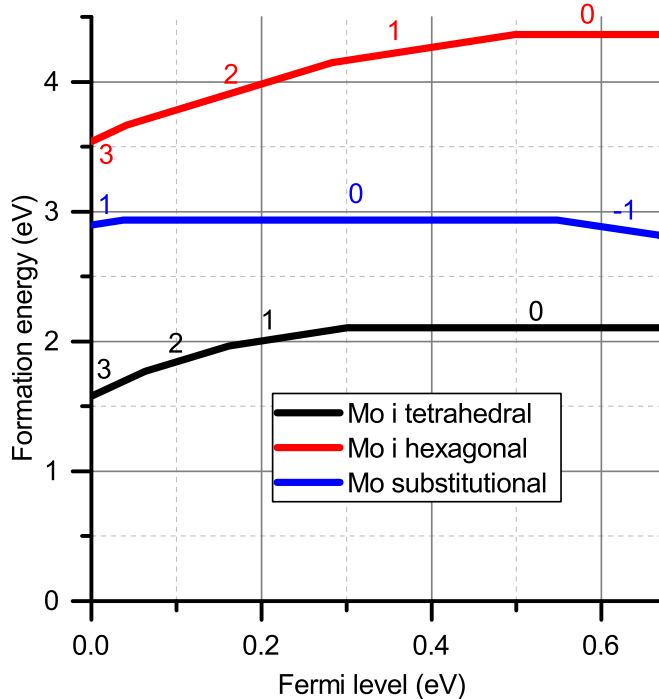


FIG. 4. Formation energy of Mo_i and Mo_{Si} defects in Si as a function of Fermi level.

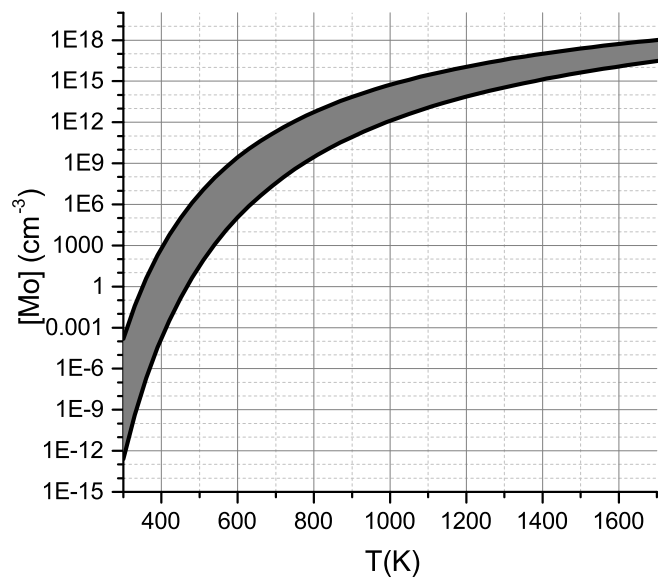


FIG. 5. Predicted range of solubility of Mo in Si as a function of temperature.

similar to V and Cr, as could be expected given their proximity on the periodic table.

The formation energy of the most favored Mo defect in Fig. 4 has a minimum value of 1.58 eV at the VBM and a maximum of 2.10 eV at higher Fermi levels. This means that *p*-type Si may allow greater defect concentrations than intrinsic or *n*-type Si due to its lower Fermi level. Using these values, Eq. (3) was used to establish a lower and upper bound of the predicted solubility of Mo in Si as a function of temperature, as shown in Fig. 5.

The efficiency of Si solar cells containing $> 10^{12}$ Mo atoms/cm³ has been known to decrease significantly due to increased carrier recombination [2]. This contaminant concentration corresponds to $\sim 10^{-11}$ atoms per Si atom (10^{-2} ppb). From these calculations it is predicted that in the presence of a source of Mo (e.g., from wafer impurities, or from a MoO₃ carrier-selective contact layer), the Mo solubility will reach this detrimental concentration somewhere in the range between 750 and 1000 K. Commonly used firing techniques for Ag screen printed pastes in solar cells are conducted at temperatures between 775 and 1175 K [55–57], falling within the temperature range in which potential Mo contamination of Si could occur.

III. DIFFUSIVITY OF Mo ATOMS

A. Mo interstitial diffusivity

Figure 6 shows the location of the equivalent sites for the tetrahedral (dark red) and hexagonal (light red) sites in the Si unit cell. Since these are the only two stable interstitial sites, at most three types of jumps need to be considered: hexagonal to hexagonal jumps, tetrahedral to hexagonal jumps and tetrahedral to tetrahedral jumps. However, this can be simplified with a closer look at the jump network. First, it is evident that a tetrahedral-tetrahedral jump can only occur via a hexagonal site. Second, it can be assumed that the

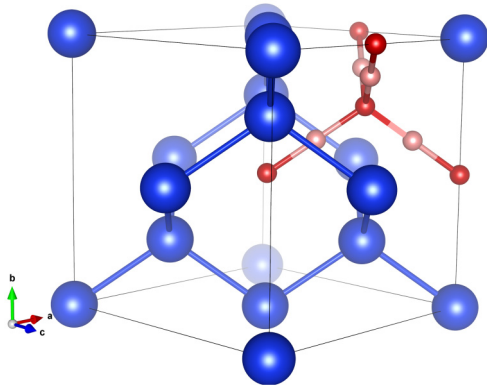


FIG. 6. Interstitial sites for Mo in Si, with tetrahedral sites in dark red and hexagonal sites in light red. The tetrahedral and hexagonal sites are connected by red lines for ease of viewing. Only the interstitial sites in the top right section of the unit cell are shown for ease of viewing.

hexagonal-hexagonal jump will go through the tetrahedral site given its close proximity and significantly lower energy. Consequently only one jump needs to be considered: the tetrahedral to hexagonal jump. Given that the hexagonal site is midway in between tetrahedral sites, Marinopolous *et al.* [14] made the assumption that the hexagonal site acts as a transition state for tetrahedral to tetrahedral jumps.

NEB calculations for Mo interstitial jumps for both charged and charge neutral states are shown in Fig. 7. The energy of the transition state was only 0.02 eV and 0.01 eV above the hexagonal site for the charge 0 and charge +1 calculations, respectively. This means that for most practical purposes, the assumption can be made that the hexagonal

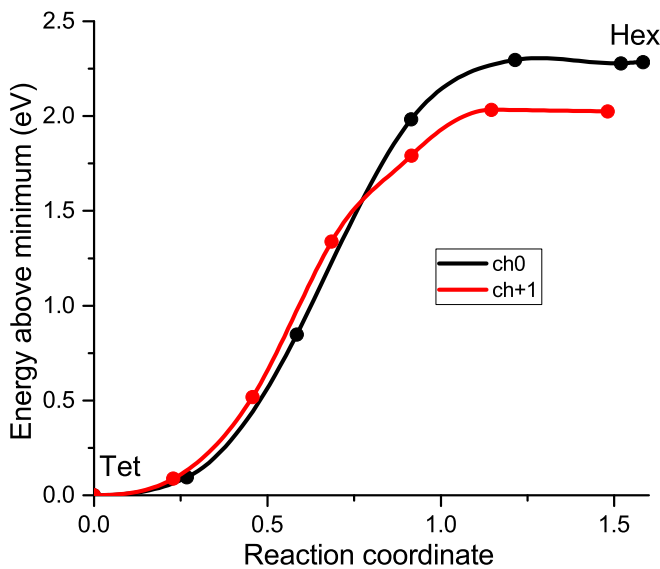


FIG. 7. Charged and uncharged interstitial NEB jumps for Mo. Red: charge neutral tetrahedral-tetrahedral jump, Black: charge neutral tetrahedral-hexagonal jump. Green: charge +1 tetrahedral-tetrahedral jump. Red: charge +1 tetrahedral-hexagonal jump. The reaction coordinate is a measure of atomic movement in between images.

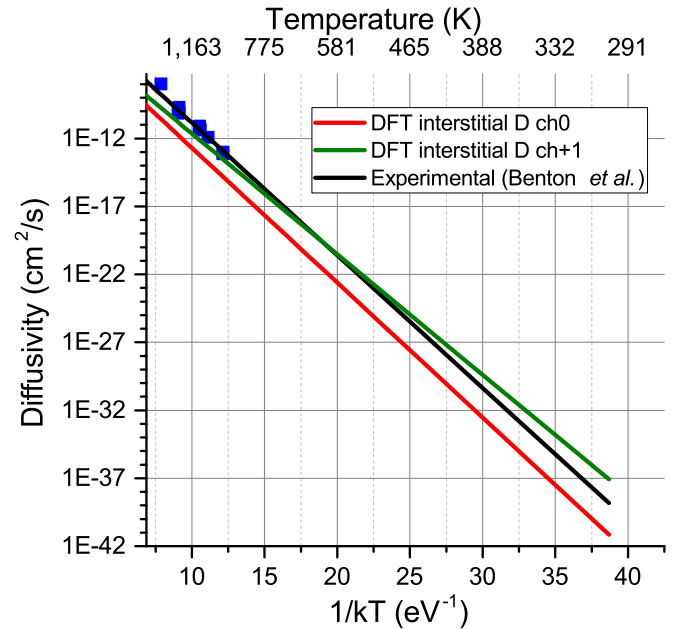


FIG. 8. Red: diffusivity of charge neutral Mo_i defects calculated through DFT. Green: Diffusivity of +1 charge Mo_i defects. Black: the diffusivity fit proposed by Benton *et al.* [5]. Blue: experimental points from Benton *et al.* [5].

site is a transition state, simplifying the required diffusivity calculations. The barrier heights measured for the tetrahedral to tetrahedral jump for the charges 0, +1, and +3 charge states are 2.29, 2.03, and 2.00 eV, respectively. This is remarkably close to the interstitial migration barrier heights of 2.31 and 2.01 eV for charges of 0 and +1, respectively, reported by Marinopolous *et al.* [14] in their DFT study using the hexagonal transition state assumption. An attempt was made to find the barrier in the +2 charge case but it did not converge despite extensive efforts, possibly due to the presence of unstable electronic configurations. Due to the fact that +1 and +3 charged defects had extremely close barriers, further analysis of positively charged Mo interstitials was restricted to the +1 charge state, under the assumption that positively charged diffusivity results would be similar.

The interstitial diffusion prefactor was calculated for the charge neutral and +1 charge jump. For the charge neutral interstitial, the attempt frequency ν^* value was found to be $(231.2/50.3) = 4.6$ THz. This corresponded to a diffusivity prefactor D_0 value of 1.7×10^3 cm²/s. Similarly, for the charge +1 state, the attempt frequency was found to be 4.0 THz, resulting in a diffusivity prefactor of 1.5×10^3 cm²/s.

Figure 8 shows the calculated interstitial diffusivity as a function of temperature for this study and the experimental (bulk, polycrystal) diffusivity of Mo in Si reported by Benton *et al.* [5]. The latter study determined an experimental diffusivity prefactor of 0.26 cm²/s and activation barrier of 2.2 eV for a temperature range between 950 and 1300 K. There appears to be good agreement between the interstitial diffusion predicted by DFT and the experimental diffusivity suggesting that, at least over this temperature range, the bulk interstitial mechanism of diffusion may be the dominant

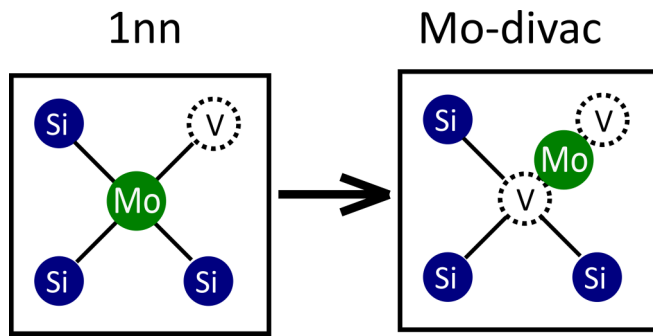


FIG. 9. Illustration of the collapse of the 1nn site into the Mo-divacancy cluster.

diffusion mechanism. The charge state of the Mo defect in the referenced experimental results was not measured, although it was most likely positively charged as the wafers were *p*-type. This is consistent with the result that the predicted diffusivity of +1 charged defects matched more closely to the experimental results than the charge neutral diffusivity. However, this cannot be stated conclusively as the uncertainty in the predicted diffusivity from the current method (in particular those associated with the exchange-correlation functional and finite size effects) may be larger than the difference between both predicted diffusivities and the experimental values. Note that the accuracy of harmonic transition state theory is known to be highest at lower temperatures, so this level of agreement at high temperatures implies that the results for this diffusion mechanism are likely to apply across lower temperatures as well.

These results predict that the positively charged Mo_i defects will diffuse faster than the charge neutral Mo_i , especially

at lower temperatures. Since positively charged Mo_i defects are dominant at low Fermi levels (see Fig. 4), this implies that it may be easier to getter Mo defects in *p*-type wafers than in intrinsic or *n*-type Si wafers, assuming there are no strong binding interactions between Mo_i and the dopant. This could be tested experimentally by comparing the diffusivity of Mo in *p*-type Si wafers with that in *n*-type Si wafers.

B. Mo inter-vacancy binding

The binding energy of two defects, A and B, into a cluster AB can be calculated with the following equation:

$$E_{\text{binding}} = E_{f(AB)} - (E_{f(A)} + E_{f(B)}). \quad (12)$$

From this equation, the energy required to bind a Mo interstitial to a Si vacancy in the form of an Mo_{Si} substitutional defect was calculated to be -2.9 eV, indicating that it is favorable for the Mo defects to become substitutional if a vacancy is already present in the material. Note that it is still more thermodynamically favorable overall to form Mo_i than Mo_{Si} , with the Mo_{Si} only becoming more favorable to form if a vacancy already exists near the defect.

To investigate whether larger Mo-vacancy clusters may form, simulations were conducted with increasing numbers of vacancies, up to four, surrounding the Mo substitution in the nearest neighbor positions. Figure 10(a) shows the formation energy of each of these configurations, and Fig. 10(b) shows the binding energy required to add one additional Si vacancy to the previous cluster configuration. The $\{Mo_{Si} : V_{Si}\}$ cluster, which has two total vacancies if the original substitution is included, is strongly favored compared to dilute, non-interacting, Mo_{Si} and V_{Si} . An interesting finding was that in this cluster, the Mo atom does not occupy its original site, instead it forms a configuration where the Mo atom sits in

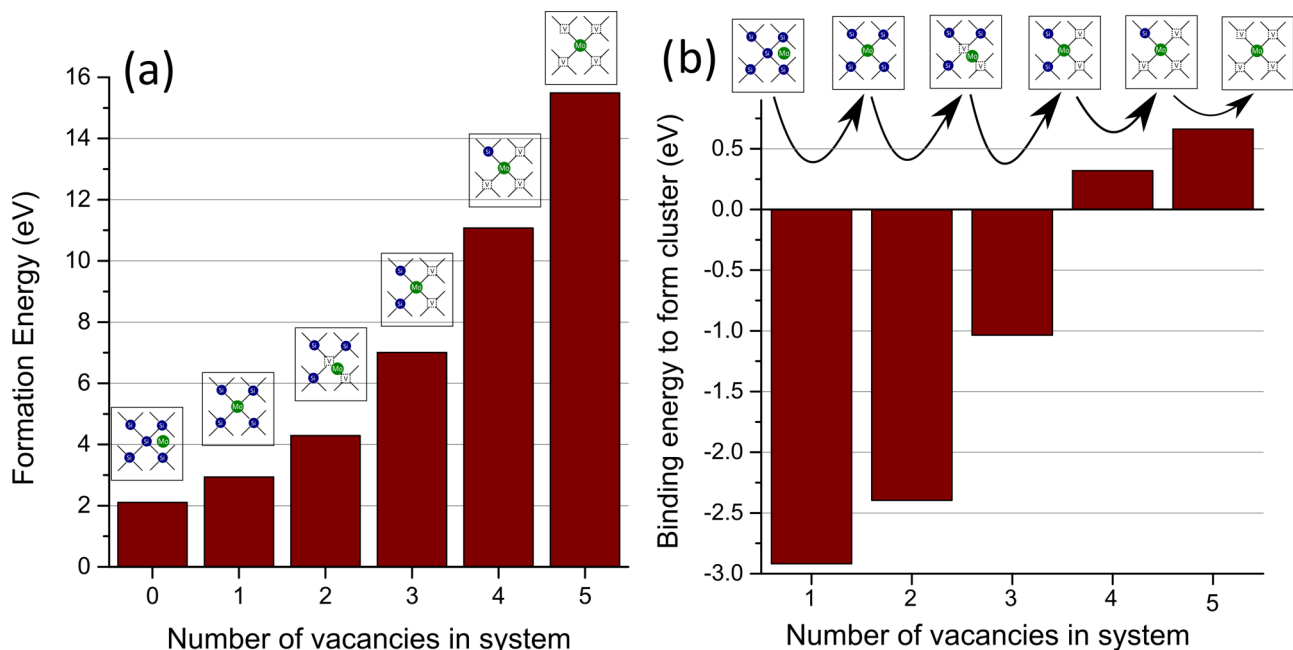


FIG. 10. (a) The formation energy for clusters of Mo with up to 5 total vacancies. (b) The binding energy required to form Mo-vacancy clusters with increasing number of vacancies from a free vacancy and the configuration with one less vacancy. In the case of Mo_{Si} , the reference configuration for the binding calculation is an Mo interstitial in the tetrahedral site.

between two vacancies, as shown in Fig. 9. This will be referred to as a Mo-divacancy cluster. This behavior has been observed in other over-sized solutes in smaller host crystal lattices, such as Y in Fe [58]. In the case of Mo in Si, the configuration appears subtly more complex, where the symmetry appears to be broken by displacements of the Mo atom in a direction normal to the vacancy-vacancy axis. More precise details about the Wyckoff location of these sites are included in Appendix A.

The addition of another vacancy is also favorable, but the gain in energy becomes smaller. This extra vacancy adds on to the divacancy configuration in the nearest Si site to form a cluster of Mo occupying a total of 3 Si sites. Finally, with four or more total vacancies the cluster is predicted to be unstable, even when excess vacancies are present. This implies that if plentiful vacancies are available, the Mo solute will form clusters with up to three vacancies bound with Mo, but no more. The strongly bound clusters of Mo_{Si} with vacancies provides one indicator that, when accommodated in substitutional sites, Mo may not diffuse quickly.

C. Vacancy-mediated diffusion

To further investigate and quantify the rate of diffusion of Mo via a vacancy-mediated mechanism, DFT calculations were performed to inform the jump barrier and attempt frequencies of the four-frequency model outlined in Sec. II C.

Vacancies in the 2 nn, 3 nn, and 5 nn sites from Fig. 1 were found to be stable under charge neutral conditions. A charge -2 simulation of the 2 nn site collapsed into the Mo-divacancy cluster, indicating that the binding of this configuration is so negative that vacancy diffusion jumps from this configuration are very unlikely to occur. For this reason, all vacancy-mediated diffusion calculations were performed under charge neutral conditions.

Figure 11 shows the binding energy of a $\{\text{Mo}_{\text{Si}} : \text{V}_{\text{Si}}\}^{\times}$ cluster with increasing distance between Mo and V (where the reference defects are taken as charge neutral). The most compact configuration, the Mo-divacancy cluster, has a very negative binding energy of -2.40 eV. The attraction decreases markedly with increasing $\text{Mo}_{\text{Si}}-\text{V}_{\text{Si}}$ distance, although there is still some binding present for vacancies at the 3 nn and 5 nn sites, indicating that the four-frequency model (which assume these are unbound) will underestimate the binding of the vacancy to the Mo impurity, and hence overestimate the diffusivity.

To determine the diffusivity, NEB simulations were used to calculate the jump height of the four frequencies as described in Sec. II C and shown in Fig. 12. The ω_2 (vacancy-solute exchange jump) in this case was approximated to be a jump between neighboring Mo-divacancy configurations (see Appendix B for a detailed explanation).

The jump from the Mo-divacancy cluster to the 2 nn site has a very high migration barrier, however the barrier of the reverse jump is very low, implying that vacancies that reach the 2 nn position are energetically favored to fall into the Mo-divacancy cluster. The ω_0 jump (Si vacancy in the bulk crystal, far from any solute) exhibits a very low migration barrier of 0.10 eV, similar to the value of 0.11 eV reported in a DFT study by Jiang *et al.* [59] This makes it very easy

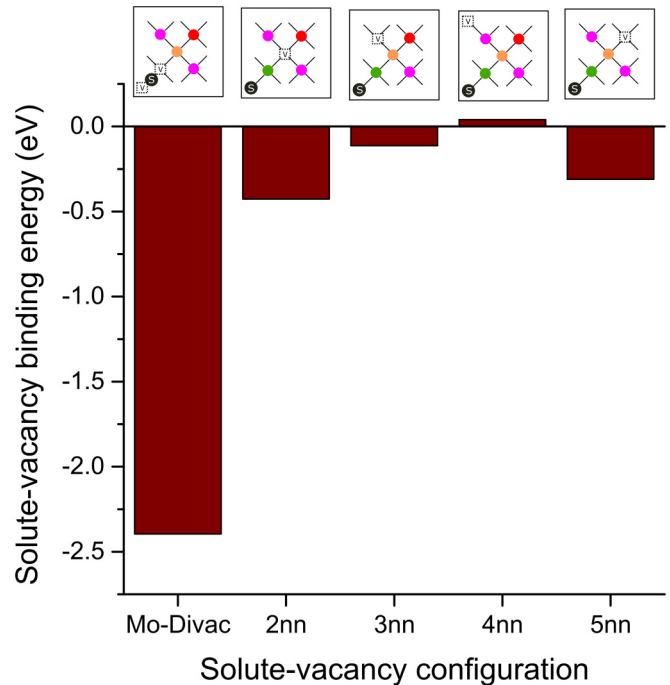


FIG. 11. Binding energy of $\{\text{Mo}_{\text{Si}} : \text{V}_{\text{Si}}\}^{\times}$ clusters for the different solute-vacancy configurations. The 1 nn configuration collapses into a Mo-divacancy cluster.

for vacancies to diffuse through Si. Note, however, that the tracer self-diffusivity of Si is not remarkably fast, since the equilibrium concentration of vacancies in Si is relatively low owing to the high formation energy of vacancies (~ 3.5 eV as calculated in Sec. III and shown in Fig. 3).

Using the ω jump definitions defined above and shown in Fig. 1, Eqs. (7)–(11) were used to calculate the vacancy-mediated diffusivity of Mo in Si. The result is shown in Fig. 13, along with the calculated [from Eq. (7)] and experimental vacancy self-diffusivity of Si.

The interstitial and vacancy mediated diffusivity can also be combined into a single total concentration-weighted diffusivity using:

$$D_{\text{total}} = \frac{c_{\text{int}}D_{\text{interstitial}} + c_{\text{sub}}D_{\text{vac-mediated}}}{c_{\text{int}} + c_{\text{sub}}}, \quad (13)$$

where c_{int} and c_{sub} are the concentrations of interstitials and substitutional Mo defects, respectively, calculated from Eq. (3) using the formation energies of Mo_{Si} and Mo_i defects. The predicted combined diffusivity is also shown in Fig. 13.

The similarity of the vacancy-mediated Mo diffusivity to the vacancy-mediated self diffusivity arises from the fact that the most important barrier to diffusion in both cases is the formation of vacancies. While the vacancy-mediated diffusivity component approaches the interstitial diffusivity component at higher temperatures, even at the Si melting temperature of 1687 K the combined diffusivity value is less than 0.4% of the interstitial diffusivity shown in Fig. 8. It can therefore be predicted that the diffusion of Mo in Si will essentially always occur via the interstitial mechanism. The assumptions about ω_2 were tested by varying the value of ω_2 over three orders of magnitude, with no effect on these conclusions.

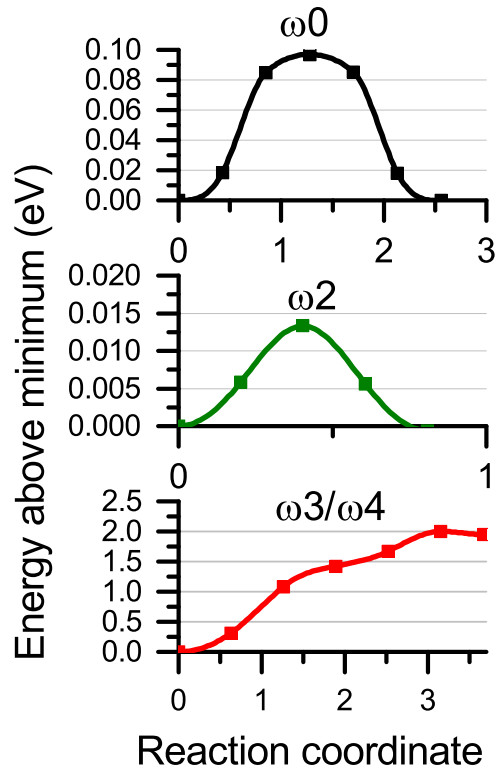


FIG. 12. The results of NEB jumps for: (a) ω_0 jump, (b) ω_2 jump, and (c) ω_3/ω_4 jump.

This eliminates the possibility that the slope of the diffusivity curve could increase at certain temperatures, maintaining the consistent difficulty of getting Mo defects. This analysis is unlikely to change when considering charged defects, as it was

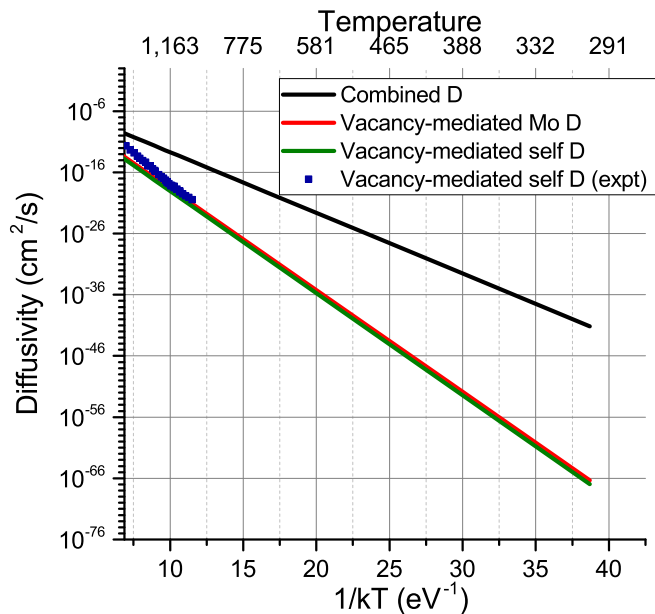


FIG. 13. Comparison of predicted substitutional (red) and total (black) diffusion of Mo defects in Si. The interstitial-only diffusivity would overlap entirely with the combined diffusivity (black line). The vacancy mediated self-diffusivity is also shown, as theoretically calculated (green) and experimentally from Shimizu *et al.* [60] (blue).

established in Sec. III A that the charge +1 Mo interstitial diffuses faster than the charge-neutral counterpart, while the -2 charge Mo substitutional appears slower than the charge neutral counterpart, implying that the dominance of interstitial migration over vacancy-mediated migration is even more pronounced for charged defects.

IV. CONCLUSIONS

Molybdenum contamination of Si at defect concentrations greater than 10^{12} atoms/cm³ can severely impact solar cell energy conversion efficiencies and, as solar cell efficiencies increase, cells become increasingly more sensitive to carrier recombination arising from impurities in the crystalline Si absorber of the cell. Contamination may arise either from Si feedstock contamination or from the use of carrier-selective contact layers such as MoO₃, the latter being of particular interest due to potential increments in cell efficiency. Although other common Si feedstock impurities (e.g., Fe) have been extensively studied using first principles methods, very few studies have reported the diffusion mechanisms of Mo in crystalline Si. This study sought to address this gap in knowledge using DFT simulations of Mo contamination and diffusion in Si.

The DFT-calculated simulations of Mo_i defects determined that only the tetrahedral and hexagonal interstitial sites were stable for Mo in crystalline Si. The calculated formation energies showed that Mo is preferentially accommodated as an interstitial species, and that the tetrahedral site is the most energetically favorable site over the entire Fermi level range in Si. The concentration of Mo defects in Si was predicted to reach levels above 20 ppt at temperatures between 750 and 1000 K. These defect concentrations are expected to be detrimental to cell performance, thereby raising concerns when high temperature Si solar cell processing steps, such as the firing of screen-printed pastes for metal contact formation, are required.

The mechanics of interstitial Mo diffusion were examined in detail. It was found that the hexagonal site acts as a transition site for jumps between Mo defects in tetrahedral interstitial sites. The resulting diffusivity equations were found to be $0.0017\exp(-2.285\text{ eV}/kT)\text{ cm}^2/\text{ s}$ for charge neutral diffusion and $0.0015\exp(-2.033\text{ eV}/kT)\text{ cm}^2/\text{ s}$ for Mo with a charge of +1. These interstitial diffusivity estimates were found to match within an order of magnitude previously reported experimental diffusivity results measured at temperatures ranging between 950 and 1300 K, suggesting that interstitial diffusion is dominant over this temperature range. The increased diffusivity for positively charged interstitial jumps implies that getting may be easier in Si with lower Fermi levels (e.g., *p*-type Si).

Binding energy calculations identified that if silicon vacancies are already present in the vicinity of Mo_i, it is favorable to form clusters of up to three vacancies bound with the Mo atom. identified that Mo_i was likely to form clusters with available Si vacancies. In particular, a cluster formed of two vacancies and a Mo atom occupying the space in between them was found to be highly stable. The strong binding of Mo_{Si} to vacancies, makes it difficult for vacancies to escape (from the complex) after binding. The resulting predicted

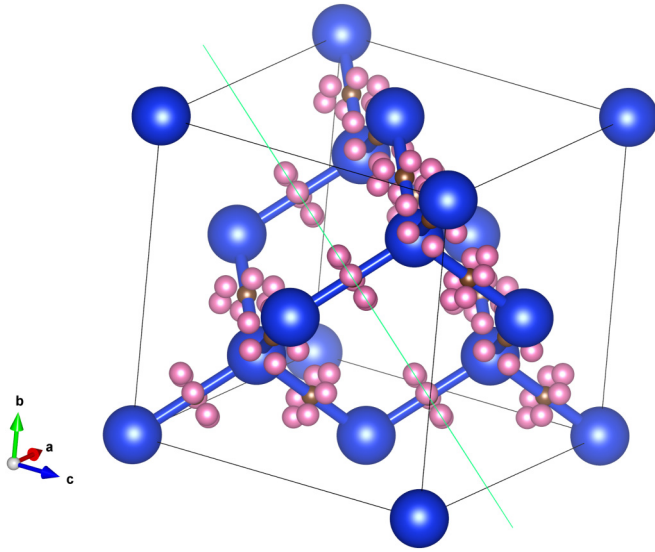


FIG. 14. Illustration of the two stable Mo sites in the Mo-divacancy configuration, with pink spheres corresponding to the G sites and brown spheres corresponding to middle sites. The green line is the (111) plane.

vacancy-mediated diffusivity was found to be negligible over all temperature ranges relevant to solar cell processing, ruling out the possibility that the dominant mechanism of diffusion could switch to vacancy-mediated and change at higher temperatures. These findings also indicate that the high temperature diffusivity measurements of Benton *et al.* [5] are likely to also be representative at lower temperatures, with no changes in diffusion mechanism.

Future work could attempt to confirm the calculated diffusivities by intentionally contaminating one surface of a wafer at different temperatures and recording elemental profiles as a function of time. The differing Mo contamination likelihood in *p*-type and *n*-type Si could also be tested experimentally by measuring the concentration of Mo in *p*-doped (low Fermi level) and *n*-doped (high Fermi level) Si wafers that are intentionally contaminated with Mo. Finally, and of particular interest to solar cell engineering, contaminating Mo defect energies could be related to recombination rates and hence to minority carrier lifetime measurements in Si wafers.

APPENDIX A: PROPERTIES OF Mo-DIVACANCY CLUSTER

As mentioned in Sec. III B, solute vacancy configurations where the vacancy is next to the solute are not stable for Mo solutes in Si. Instead, these simulations collapse into a Mo-divacancy configuration. This Mo-divacancy cluster has several interesting properties. First, it is found to have a stable and a metastable position, shown in Fig. 14. In the metastable configuration, which will be referred to as the middle site, Mo lies directly halfway in between the two vacancy sites. A second position that Mo can occupy, which will be referred to as the G site, is close to the middle site but slightly displaced along one of six $\langle 110 \rangle$ directions normal to the axis connecting the two vacancies. The G site is equidistant from both vacancies, occupying the Wyckoff 96g site and unit cell coordinates (0.159, 0.159, 0.057). The G sites are lower in energy than the middle site by 0.25 eV. In this study, it is assumed that Mo lies in a G site when in the Mo-divacancy cluster.

APPENDIX B: THE ω_2 JUMP

The ω_2 jump is defined as the exchange jump between a substitutional solute and a nearby vacancy. There is some difficulty in identifying the ω_2 jump for the specific case of vacancy mediated Mo diffusion in Si, due to the 1 nn configuration being unstable. Here the argument is made that an appropriate choice for the ω_2 jump is the jump between neighboring G sites in the Mo-divacancy configuration.

As shown in Fig. 15, the Mo-divacancy configuration has six available G sites. In a static configuration these are symmetrically equivalent, but this is not the case with respect to a jump out to a particular 2 nn site. Mo-divacancy to 2 nn jumps were attempted for several jumps out to a specific site, and it was found that in order for the jump to occur, the Mo atom must first migrate to the G site that is physically closest to the 2 nn site to which the vacancy is jumping. For example, in Fig. 15, the red atom is in the correct position for the vacancy labeled 1 to jump to site a, but not in the correct position for the vacancy labeled 2 to jump to site b. This means that in order for an exchange to occur, a jump from one G site to a neighboring G site is necessary.

The G site to G site jump is not exactly topologically equivalent to the ω_2 jump of the four-frequency model. For

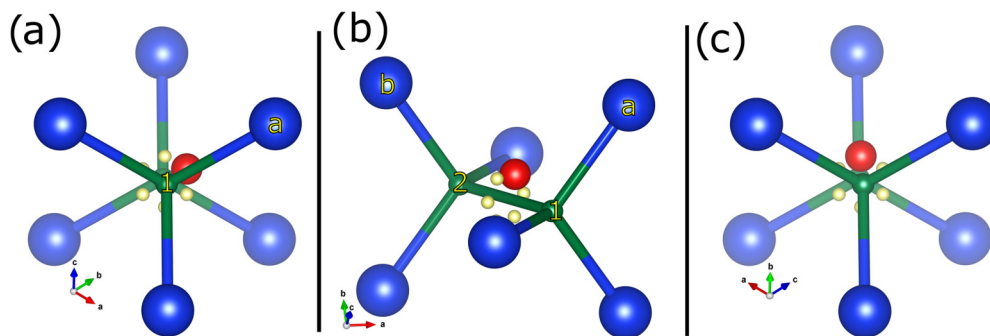


FIG. 15. Illustration of the asymmetry between jumps with the Mo in different G sites, showing the same atoms from three different angles. Green: vacancy sites, labeled 1 and 2. Blue: Si sites in the 2 nn position. Red: specific Mo atom in a G site. Yellow: other G sites.

the G site arrangement there are six equivalent vacancy-solute 1 nn sites with each configuration allowing a vacancy to escape to only one neighboring site, while in the more typical arrangement there are two 1 nn equivalent sites allowing three escape jumps (ω_3) each. However, the G site to G site jumps have remarkably low energy barrier—two orders of magnitude lower than the ω_3 escape jumps. This means that the exponential term in Eq. (5) is close to unity, leaving the attempt frequency as the limiting factor in the

frequency of exchange. In this limiting case the exchange jump frequency is approximately five orders of magnitude greater than that of the ω_3 jump. It is therefore reasonable to assume that all six ω_3 jumps are equally available from the 1 nn configuration, irrespective of whether these are G site type configurations or conventional configurations. For these reasons, approximating the ω_2 jump as a G site to G site jump should not introduce significant errors into the results.

-
- [1] J. Davis, A. Rohatgi, P. Rai-Choudhury, P. Blais, R. Hopkins, and J. McCormick, in *Proceedings of the 13th Photovoltaic Specialists Conference* (IEEE, Piscataway, NJ, 1978), p. 490.
- [2] A. Rohatgi, R. H. Hopkins, J. R. Davis, R. B. Campbell, and H. C. Mollenkopf, *Solid State Electron.* **23**, 1185 (1980).
- [3] G. Coletti, L. Geerligs, P. Manshanden, C. Swanson, S. Riepe, W. Warta, J. Arumughan, and R. Kopecek, in *Solid State Phenomena* (Trans Tech Publications, Zurich, 2008), p. 15.
- [4] A. R. Peaker *et al.*, *Phys. Status Solidi (a)* **209**, 1884 (2012).
- [5] J. Benton, D. Jacobson, B. Jackson, J. Johnson, T. Boone, D. Eaglesham, F. Stevie, and J. Becerro, *J. Electrochem. Soc.* **146**, 1929 (1999).
- [6] D. Macdonald and L. Geerligs, *Appl. Phys. Lett.* **85**, 4061 (2004).
- [7] J. Davis, A. Rohatgi, R. H. Hopkins, P. D. Blais, P. Rai-Choudhury, J. R. McCormick, and H. Mollenkopf, *IEEE Trans. Electron Devices* **27**, 677 (1980).
- [8] A. Istratov, T. Buonassisi, R. McDonald, A. Smith, R. Schindler, J. Rand, J. P. Kalejs, and E. Weber, *J. Appl. Phys.* **94**, 6552 (2003).
- [9] C. Battaglia, S. M. De Nicolas, S. De Wolf, X. Yin, M. Zheng, C. Ballif, and A. Javey, *Appl. Phys. Lett.* **104**, 113902 (2014).
- [10] J. Geissbühler *et al.*, *Appl. Phys. Lett.* **107**, 081601 (2015).
- [11] T. Hamaguchi and Y. Hayamizu, *Japan. J. Appl. Phys.* **30**, L1837 (1991).
- [12] F. Beeler, O. K. Andersen, and M. Scheffler, *Phys. Rev. B* **41**, 1603 (1990).
- [13] F. Beeler, O. K. Andersen, and M. Scheffler, *Phys. Rev. Lett.* **55**, 1498 (1985).
- [14] A. G. Marinopoulos, P. Santos, and J. Coutinho, *Phys. Rev. B* **92**, 075124 (2015).
- [15] Z. Z. Zhang, B. Partoens, K. Chang, and F. M. Peeters, *Phys. Rev. B* **77**, 155201 (2008).
- [16] A. Sharan, Z. Gui, and A. Janotti, *Phys. Rev. Appl.* **8**, 024023 (2017).
- [17] J. M. Ziman, *Principles of the Theory of Solids* (Cambridge University Press, Cambridge, 1979).
- [18] M. N. Afsar and K. J. Button, *IEEE Trans. Microwave Theory Tech.* **31**, 217 (1983).
- [19] S. T. Murphy and N. D. Hine, *Chem. Mater.* **26**, 1629 (2014).
- [20] V. Milman, M. C. Payne, V. Heine, R. J. Needs, J. S. Lin, and M. H. Lee, *Phys. Rev. Lett.* **70**, 2928 (1993).
- [21] M. Mantina, Y. Wang, L. Q. Chen, Z. K. Liu, and C. Wolverton, *Acta Mater.* **57**, 4102 (2009).
- [22] G. Henkelman, B. P. Uberuaga, and H. Jónsson, *J. Chem. Phys.* **113**, 9901 (2000).
- [23] G. H. Vineyard, *J. Phys. Chem. Solids* **3**, 121 (1957).
- [24] D. Andersson *et al.*, *J. Nucl. Mater.* **451**, 225 (2014).
- [25] H. Wu, T. Mayeshiba, and D. Morgan, *Scientific Data* **3**, 160054 (2016).
- [26] T. Garnier, V. R. Manga, D. R. Trinkle, M. Nastar, and P. Bellon, *Phys. Rev. B* **88**, 134108 (2013).
- [27] R. Agarwal and D. R. Trinkle, *Phys. Rev. Lett.* **118**, 105901 (2017).
- [28] R. Agarwal and D. R. Trinkle, *Acta Mater.* **150**, 339 (2018).
- [29] C. Freysoldt, B. Grabowski, T. Hickel, J. Neugebauer, G. Kresse, A. Janotti, and C. G. Van de Walle, *Rev. Mod. Phys.* **86**, 253 (2014).
- [30] S. Hu, *Phys. Status Solidi (b)* **60**, 595 (1973).
- [31] J. R. Manning, *Phys. Rev. B* **6**, 1344 (1972).
- [32] M. Mantina, Y. Wang, R. Arroyave, L. Q. Chen, Z. K. Liu, and C. Wolverton, *Phys. Rev. Lett.* **100**, 215901 (2008).
- [33] A. Le Claire, *J. Nucl. Mater.* **69**, 70 (1978).
- [34] M. Mantina, L. Q. Chen, and Z. K. Liu, in *Defect and Diffusion Forum* (Trans Tech Publications, Zurich, 2009), p. 1.
- [35] L. Messina, M. Nastar, N. Sandberg, and P. Olsson, *Phys. Rev. B* **93**, 184302 (2016).
- [36] D. Tsuchiya, K. Sueoka, and H. Yamamoto, *Phys. Status Solidi (a)* **216**, 1800615 (2019).
- [37] L. Du, Z. Wu, S. Li, Z. Hu, and Y. Jiang, *Solid State Commun.* **226**, 1 (2016).
- [38] D. J. Backlund, T. M. Gibbons, and S. K. Estreicher, *Phys. Rev. B* **94**, 195210 (2016).
- [39] J. Dabrowski and G. Kissinger, *Phys. Rev. B* **92**, 144104 (2015).
- [40] F. Legrain, O. I. Malyi, and S. Manzhos, *Comput. Mater. Sci.* **94**, 214 (2014).
- [41] S. K. Estreicher, D. J. Backlund, C. Carbogno, and M. Scheffler, *Angew. Chem. Int. Ed.* **50**, 10221 (2011).
- [42] F. Corsetti and A. A. Mostofi, *Phys. Rev. B* **84**, 035209 (2011).
- [43] P. Rinke, A. Janotti, M. Scheffler, and C. G. Van de Walle, *Phys. Rev. Lett.* **102**, 026402 (2009).
- [44] M. I. J. Probert and M. C. Payne, *Phys. Rev. B* **67**, 075204 (2003).
- [45] W.-K. Leung, R. J. Needs, G. Rajagopal, S. Itoh, and S. Ihara, *Phys. Rev. Lett.* **83**, 2351 (1999).
- [46] Y. Mo, M. Z. Bazant, and E. Kaxiras, *Phys. Rev. B* **70**, 205210 (2004).
- [47] E. R. Batista, J. Heyd, R. G. Hennig, B. P. Uberuaga, R. L. Martin, G. E. Scuseria, C. J. Umrigar, and J. W. Wilkins, *Phys. Rev. B* **74**, 121102(R) (2006).
- [48] A. F. Wright, *Phys. Rev. B* **74**, 165116 (2006).
- [49] S. L. Dudarev, G. A. Botton, S. Y. Savrasov, C. J. Humphreys, and A. P. Sutton, *Phys. Rev. B* **57**, 1505 (1998).
- [50] P. E. Blöchl, O. Jepsen, and O. K. Andersen, *Phys. Rev. B* **49**, 16223 (1994).
- [51] P. A. Schultz, *Phys. Rev. Lett.* **96**, 246401 (2006).

- [52] P. E. Blöchl, E. Smargiassi, R. Car, D. B. Laks, W. Andreoni, and S. T. Pantelides, *Phys. Rev. Lett.* **70**, 2435 (1993).
- [53] F. E. Rougieux, C. Sun, and D. Macdonald, *Sol. Energy Mater. Sol. Cells* **187**, 263 (2018).
- [54] H. Pettersson, H. G. Grimmeiss, L. Tilly, K. Schmalz, K. Tittelbach, and H. Kerkow, *Semicond. Sci. Technol.* **6**, 237 (1991).
- [55] S. Rane, P. Khanna, T. Seth, G. Phatak, D. Amalnerkar, and B. Das, *Mater. Chem. Phys.* **82**, 237 (2003).
- [56] T. Dullweber, S. Gatz, H. Hannebauer, T. Falcon, R. Hesse, J. Schmidt, and R. Brendel, *Prog. Photovoltaics Res. Appl.* **20**, 630 (2012).
- [57] J. D. Fields, M. I. Ahmad, V. L. Pool, J. Yu, D. G. Van Campen, P. A. Parilla, M. F. Toney, and M. F. A. M. van Hest, *Nat. Commun.* **7**, 11143 (2016).
- [58] J.-L. Bocquet, C. Barouh, and C.-C. Fu, *Phys. Rev. B* **95**, 214108 (2017).
- [59] M. Jiang, H. Xiao, S. Peng, G. Yang, Z.-J. Liu, L. Qiao, and X. Zu, *A Theoretical Simulation of the Radiation Responses of Si, Ge, and Si/Ge Superlattice to Low-Energy Irradiation* (National Center for Biotechnology Information, Bethesda, MD, 2018), Vol. 13.
- [60] Y. Shimizu, M. Uematsu, and K. M. Itoh, *Phys. Rev. Lett.* **98**, 095901 (2007).